

Localization of large intraplate earthquakes along faulted density-contrast boundaries: Insights from the 2017 Mw6.5 Botswana earthquake



Chikondi Chisenga^{a,*}, Folarin Kolawole^b, Tahiry Rajaonarison^c, Estella A. Atekwana^d,
Jianguo Yan^e, Elisha M. Shemang^f

^a Department of Earth Sciences, Ndata School of Climate and Earth Sciences, Malawi University of Science and Technology, P.O. Box 5196, Limbe, Malawi

^b Department of Earth and Environmental Sciences, Lamont-Doherty Earth Observatory of Columbia University, New York, USA

^c Earth and Environmental Science, New Mexico Institute of Mining and Technology, Socorro, USA

^d Department of Earth and Planetary Sciences, University of California, Davis, One Shields Ave, Davis, CA, 95616, USA

^e State Key Laboratory of Information Engineering in Surveying, Mapping and Remote Sensing, Wuhan University, Box 129, Luoyu Road, Wuhan, China

^f Department of Earth and Environmental Sciences, Botswana International University of Science and Technology, Palapye, Botswana

ARTICLE INFO

Keywords:

Intraplate earthquake
Lower crust
Gravity inversion
Density
Fault reactivation
Limpopo-shashe belt

ABSTRACT

The major controls on the localization of deep crustal intraplate earthquakes remain enigmatic due to their deep hypocentral depths and rarity of coseismic surface ruptures. Here, we investigate the 3-D crustal density structure of the 2017 Mw 6.5 Botswana earthquake epicentral region, a strong lower-crustal (~24–29 km) event which is suspected to have reactivated a Precambrian structure via normal faulting. We perform a 3-D inversion of the gravity data using published geological constraints, then integrate the resulting density model with aftershock hypocenter distribution and use as constraints in a 3-D thermo-mechanical geodynamic model implemented in ASPECT. Our results reveal crustal blocks of density anomalies, with the aftershocks clustering along a prominent NW-trending, NE-dipping density contrast separating a high-density (>2708 kg/m³) footwall and lower-density (2670–2700 kg/m³) hanging wall blocks. Additionally, a secondary density contrast boundary in the hanging wall coincides with a splay of aftershock clusters at depth. Our observations suggest that the 2017 Mw6.5 Botswana earthquake nucleated near a fault intersection in the lower crust and is associated with brittle normal faulting reactivation of a long-lived basement fault that follows a prominent deep-reaching density contrast boundary. Further, as demonstrated by geodynamic modeling results, we argue that in regions of low tectonic loading rates, where stress perturbations are high enough, faulted crustal-scale density contrast boundaries are preferential concentrators of strain that may localize intraplate earthquakes.

1. Introduction

The need to better understand and characterize the crustal structure of continental cratonic environments where extremely-low tectonic loading rates dominate has been highlighted by the occurrence of devastating large magnitude intra-plate earthquakes in such environments (e.g., Talwani, 2014; Calais et al., 2016 and references therein). Examples of such large earthquake events include the 1811–1812 M7.3–7.9 New Madrid events in the central U.S. (Arch C Johnston et al., 1996); the M6.6 1988 Tennant Creek earthquakes in Australia (McCaffrey, 1989), the 2001 Mw7.7 Bhuj earthquake (Prantik Mandal and Pandey, 2010), 1886 Mw 6.9–7.3 Charleston earthquakes (Hough et al., 2003), the 2016 M5.9 northern Tanzania earthquake (USGS, 2016), and

the 2017 Mw6.5 Botswana earthquake (Kolawole et al., 2017; Gardonio et al., 2018; Midzi et al., 2018; Moorkamp et al., 2019; Materna et al., 2019; Fadel et al., 2018, 2020). Studies have demonstrated that large intraplate earthquakes may (e.g., Tesauro et al., 2015) or may not (Talwani, 2014) follow craton edges but typically nucleate within and reactivate ancient zones of weaknesses in intra-cratonic settings (e.g., Sykes, 1978; Johnston, 1996; Kolawole et al., 2017). Although the physics of intraplate seismic rupture in stable continental regions has been widely associated with the slow accrual of tectonic strain leading to dynamic shear failure (Kanamori and Brodsky, 2004), it is argued that such events may be primarily triggered by transient local stress perturbations without prior strain accrual (Calais et al., 2016). Examples of local stress perturbations include dynamic triggering from far-field

* Corresponding author.

E-mail address: cchisenga@must.ac.mw (C. Chisenga).

earthquakes (e.g., Hough et al., 2003) and local fluid pressurization (e.g., Balfour et al., 2015).

Large intraplate earthquakes in intraplate continental regions are rare (Talwani, 2014), and those that rupture at lower-crustal depths are even rarer. The major controls on the localization of lower crustal intraplate events remain enigmatic due to their deep hypocentral depths and lack of coseismic surface ruptures. Along active tectonic boundaries and in some intraplate regions, lower-crustal earthquakes have been associated with lithology-dependent seismogenic properties of the lower-crust (Shi et al., 2018) and the thermo-mechanical stratigraphy of the lithosphere (e.g., Chen and Molnar, 1983; Jackson, 2002; Jackson et al., 2008).

The 2017 Mw6.5 Botswana earthquake is a rare lower-crustal (24–29 km-deep) normal faulting event, which occurred in the Neo-Archean/Paleo-Proterozoic Limpopo-Shashe collisional belt, sandwiched between the Kaapvaal and Zimbabwe Cratons (Fig. 1a–b). The epicentral region (Fig. 1c), located ~350 km south of the active Okavango Rift Zone, has historically low seismicity and no record of large earthquakes (Fig. 1a; Kolawole et al., 2017). Following the 2017 earthquake, several studies of the event highlighted the roles of pre-existing basement fault structure, local stress regime, stress contrasts, fluid pressurization and strength state of the crust and upper mantle on the occurrence of the earthquake (Kolawole et al., 2017; Albano et al., 2017; Gardonio et al., 2018; Materna et al., 2019; Moorkamp et al., 2019, 2020; Fadel et al., 2020; Chisenga et al., 2020a). Kolawole et al. (2017) inferred that the seismic event resulted from the extensional reactivation of a NW-striking, NE-dipping crustal-scale Precambrian thrust splay (the Moiyabana Fault) within the Southern Marginal Zone (SMZ) of

Limpopo-Shashe Belt (Fig. 1c). Gardonio et al. (2018) suggested that the event was triggered by fluid release from the mantle that activated brittle faults in the lower crust. A low velocity upper mantle anomaly extends from the region of the East African Rift System into the epicentral region and is interpreted to represent an ascending body of melt, possibly indicating incipient rifting at the epicenter area (Fadel et al., 2020). Conversely, Materna et al. (2018) argued for a SW-dipping geometry for the causative fault. In addition, the clustering of aftershock hypocenters with normal faulting source mechanisms in the region and the presence of NW-trending Holocene fault scarps further southeast of the epicentral area suggest active low strain tectonic extension in the region (Mulabisana et al., 2021; Paulsen et al., 2022).

Previous geophysical studies attempted to image the deep crustal structure of eastern Botswana and the epicentral region using seismic and magnetotelluric studies (Miensopust et al., 2011; Khoza et al., 2013; Youssof et al., 2013; Yu et al., 2015; Fadel et al., 2018; Moorkamp et al., 2018) and inversion of aeromagnetic data (Kolawole et al., 2017). These studies indicate that eastern Botswana is underlain by thick lithosphere of the Kaapvaal and Zimbabwe Cratons (~220 km; Miensopust et al., 2011), with a relatively thinner and weaker lithosphere beneath the Limpopo-Shashe Belts (Moorkamp et al., 2019). Within the Limpopo-Shashe Belt, the crust is thicker in the Central Zone (~43 km; Yu et al., 2015; Fadel et al., 2018) and thinner in the Southern Marginal Zone (~40 km; Yu et al., 2015; Fadel et al., 2018), with an average crustal thickness of ~40 km. The lower crustal composition is commonly felsic with a Vp/Vs of ~1.75 in the Southern Marginal Zone (Fadel et al., 2018). However, these studies being regional-scale, do not provide much detail within the epicentral region.

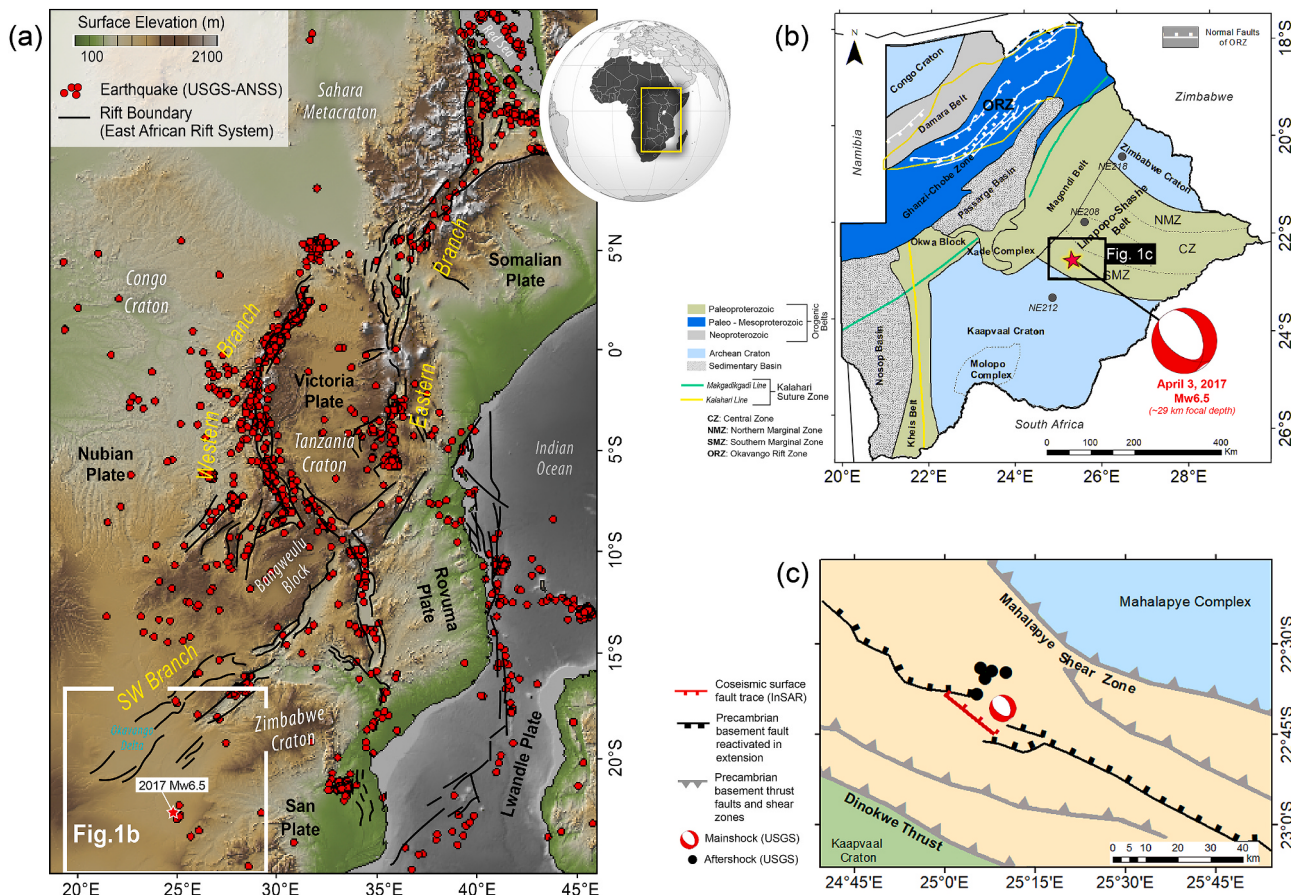


Fig. 1. (a) The location of Botswana, the study area, in relation to the East African Rift System. (b) Tectonic map of Botswana (modified after Key and Ayres, 2000; Ranganai et al., 2002; Singletary et al., 2003) showing the epicenter of the 2017 Mw6.5 earthquake. Grey circles represent locations of seismic stations used for published crustal thickness estimates (Fadel et al., 2018); the highest thickness estimate (50 km) is at NE218. (c) The 2017 Mw6.5 epicentral region in Moiyabana, showing the mainshock and aftershocks from USGS, and published basement faults from Kolawole et al. (2017).

To better understand how faults reactivate in intraplate regions, we investigate the controls of crustal structure heterogeneity and possible significance for lower-crustal intraplate brittle fault reactivation by using the 2017 Botswana earthquake as a case study. We investigate the three-dimensional (3-D) crustal density structure of Eastern Botswana with particular emphasis on the 2017 epicentral region. We present the results comparing the distribution of aftershock hypocenters with the 3-D crustal density model and test the geodynamic implications of the results with a representative 3-D thermomechanical model.

2. Geological background

Eastern Botswana hosts the Kalahari Craton which consists of two Archean cratons: the Zimbabwe Craton in the northeast and the Kaapvaal Craton in the southwest, separated by the Limpopo-Shashe Belt (Fig. 1a–b). Geochronology and radiometric dating studies suggest that the Kaapvaal Craton and the Zimbabwe Craton were formed between 3.7 Ga and 2.6 Ga (Begg et al., 2009 and references therein). The Kaapvaal Craton, which extends from southeastern/southern Botswana into South Africa, is composed of granitoids with gneisses and 3.7–2.7 Ga narrow greenstone belts. The Zimbabwe Craton, which extends from eastern Botswana into Zimbabwe, is composed of folded volcano-sedimentary sequences of greenstone belts that are associated with granites and gneisses. The Zimbabwe Craton was amalgamated to the Kaapvaal Craton through an east-directed crustal movement (Begg et al., 2009). The suture between the two cratonic nuclei is the 2.7–2.6 Ga high metamorphic grade NW-SE trending Limpopo-Shashe Belt, which extends from eastern Zimbabwe and South Africa into Botswana (Clifford, 1970). The northern boundary of the Limpopo-Shashe Belt is truncated by the NE-SW striking Paleoprotorezoic Magondi Belt.

The Limpopo-Shashe Belt is characterized by a pop-up crustal structure, which is similar to Himalaya type (Roering et al., 1992). The belt is subdivided into 3 zones: the Northern Marginal Zone (NMZ), the Central Zone (CZ), and the Southern Marginal Zone (SMZ) (Fig. 1a), based on the lithological and structural similarities (e.g., McCourt and Vearncombe, 1992). The NMZ is composed of granulite-facies rocks, mostly dominated by Charnockite and some minor occurrences of mafic rocks and banded-iron formation components. Grey gneisses associated with granulite and amphibolite-facies occur in the CZ, which have also some occurrences of pelite, quartzite and carbonate. Whereas the SMZ is predominantly a granitoid-greenstone terrane, hosting similar rocks to those that are found in northern Kaapvaal Craton. The basement rocks of SMZ, which are mostly exposed in South Africa, are predominantly made of tonalite-trondhjemite-granite assemblages and granulites (Ranganai et al., 2002). The SMZ terrane differs considerable from the geologically distinct CZ as it contains cratonic rocks. Nevertheless, all the three zone of the Limpopo-Shashe Belt contains granulite facies and noticeable crustal erosion, the CZ still shows the normal continental crust thickness (Ranganai et al., 2002).

The 2017 Botswana earthquake occurred in the SMZ, which is separated from the Kaapvaal Craton and the Central Zone by the southwest verging Dinokwe Thrust (DT) and Mahalapye Shear Zone (MsZ), respectively (Fig. 1b; Ranganai et al., 2002). Several buried NW-SE trending faults were mapped between DT and MsZ from aeromagnetic data, gravity, and Differential Interferometric Synthetic Aperture Radar (DInSAR) (Fig. 1b; Kolawole et al., 2017). The ruptured fault for the Botswana earthquake, named the Moiyabana fault, was coincident with a prominent magnetic anomaly in this region (Fig. 3 of Kolawole et al., 2017).

3. Data and methods

3.1. Gravity data

We used the Bouguer gravity data, obtained from the Botswana Geoscience Institute (BGI), with a uniform resolution of ~7.5 km, and

provided as a 1 km Bouguer anomaly grid (Fig. 2a). Previous studies have shown that the Bouguer gravity data contains enough signals to estimate the crust-mantle boundary (Fig. 2b; e.g., Leseane et al., 2015; Yu et al., 2015; Chisenga et al., 2020b), and map basement fabrics and other tectonic structures (Fig. 2c–d; e.g., Ranganai et al., 2002; Kolawole et al., 2017; Chisenga et al., 2020a). Thus, the Bouguer gravity data contains both low and high frequency signals required to recover the targeted near surface and deep subsurface structures in our study (Fig. 2b–d).

To resolve edges and their lateral continuity in the gravity anomaly grid, we apply a vertical derivative and low-pass filter to the Bouguer gravity data, providing an opportunity to investigate structural boundaries in the upper crust that may exist within the region. Such filters have been shown to delineate basement structures buried beneath the Kalahari Sands in the epicentral region (Kolawole et al., 2017). Following standard practice, mathematical derivatives are useful for resolving gradients corresponding to structural boundaries in potential fields data (e.g., Miller and Singh, 1994; Salem et al., 2007; Kolawole et al., 2018). Where the first vertical derivative of the Bouguer gravity grid resolves the high-frequency shorter-wavelength anomalies corresponding to structures in the shallow crust, the vertical derivative of a low-pass filtered Bouguer grid would resolve structural gradients of lower-frequency longer-wavelength anomalies at deeper depths in the basement (see example in Kolawole et al., 2017). Here, we assess structural gradients at shallow crustal levels in the vertical derivative of the raw Bouguer anomaly gravity grid, and structural gradients at ‘deeper’ crustal levels in the first vertical derivative of the 35 km low-pass filtered Bouguer anomaly (corresponding to >15 km equivalent depth).

To obtain gravity signals that are required to resolve the crustal density structure, the Bouguer gravity data was filtered with a 1000 km Butterworth high pass filter to approximately remove mantle contribution (e.g., Block et al., 2009). The residual gravity data was then extended into a rectangular form using Winograd Fourier Transform algorithm (Winograd, 1978, 1979) and then filled with maximum entropy method (Burg, 1975) to conform to the applied inversion algorithm.

3.2. 3-D inversion algorithm

To resolve the density crustal structure beneath Eastern Botswana, we applied a three-dimensional (3-D) density inversion to the residual Bouguer gravity data. Here, we adopted the 3-D tesseral inversion approach of Zhang et al. (2018), which is solved as the conjugate gradient (CG) matrix with an iterative function. The algorithm combines a modified version of Li and Oldenburg (1996, 1998) by Liang et al. (2014) and Lagrangian multiplier method of Zhang et al. (2015). Unlike the traditional potential fields inverse algorithm, the Lagrangian multiplier method of Zhang et al. (2015) takes full advantage of prior geological information as a constraint and thus obtains a new objective function for inversion by adding Lagrangian multipliers and slack variables to the traditional inversion method.

Gravity inversion is based on the depth weighting algorithm pioneered by Li and Oldenburg (1996, 1998). Since then, the algorithm has been extensively used to resolve density variations of different regions, both on the Earth and on the Moon (e.g., Li and Oldenburg, 1998, 1996; Jansen et al., 2017; Zhang et al., 2018; Chisenga et al., 2019, 2020b). The algorithm is ideal for deep density studies since the depth weighting function reduces clustering of density values close to the surface and counteracts the decay of gravity signal with depth. This produces a uniform distribution of density anomalies with depth. The pioneering work of Li and Oldenburg (1996, 1998) formulated the algorithm as an optimization problem that minimizes the model objective function and the data misfit in the objective function for the density model, as illustrated in Eq. (1),

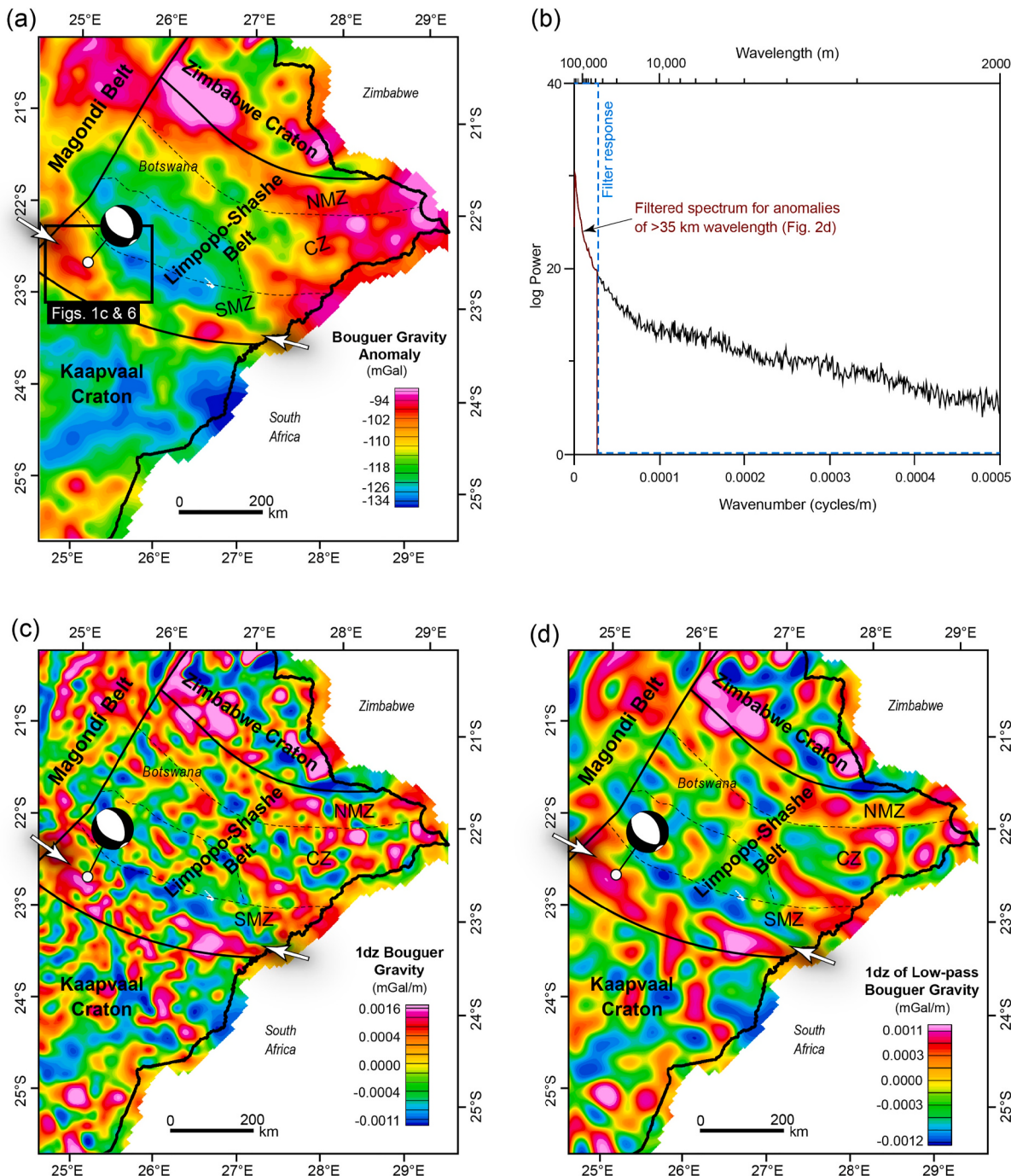


Fig. 2. (a) Bouguer anomaly map of eastern Botswana. (b) Radially averaged frequency spectrum of the Bouguer anomaly gravity data, showing the high and low wavenumber contents of the data and the section of the spectrum represented in panel d (i.e., 35 km low pass). (c) First vertical derivative of the Bouguer anomaly grid, showing the shallow crustal anomaly gradients. (d) First vertical derivative of the 35 km low-pass filtered Bouguer anomaly grid showing the longer-wavelength (corresponding to >15 km equivalent depth) anomalies and their vertical gradients.

$$\mathcal{O}(m) = \mathcal{O}_d + \mu \mathcal{O}_m \quad (1)$$

where: $\mathcal{O}(m)$ is the objective function, \mathcal{O}_d is the data misfit, \mathcal{O}_m is the model objective function and μ is the regularization parameter. The data misfit (\mathcal{O}_d) was constructed to determine the tradeoff between the calculated data from density model and the observed data, as illustrated by Eq (2),

$$\mathcal{O}_d = \|W_d(Gm - d^{obs})\|_2^2 \quad (2)$$

This measure of data misfit (\mathcal{O}_d) represented a 2-norm measure (Eq

(2); Li and Oldenburg, 1996, 1998), where W_d is a data weighing matrix, and G is the kernel function that defines the relationship between the geological model (m) and the observed data (d^{obs}). Conversely, the model objective function (\mathcal{O}_m) works as a balance between the physical properties of the reference model and the desired density model, as given by Eq (3),

$$\mathcal{O}_m = \|W_m(m - m_{ref})\|_2^2 \quad (3)$$

In Eq (3), W_m is also a weighting matrix for the model objective function, which defines how close the recovered model (m) is to the

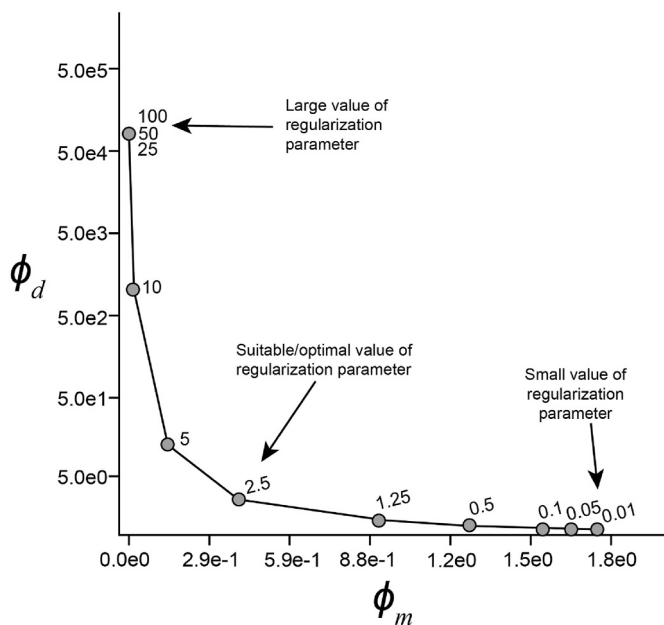


Fig. 3. L-curve solution for data misfit (ϕ_d) against model objective function (ϕ_m). The plot, called the L-curve method (Lawson and Hanson, 1974), indicates the optimal value of regularization parameter as a value that lies at the corner of the L-curve.

reference model (m_{ref}). The model objective function (ϕ_m), which is sometimes referred to as a model norm, measures the smoothness of the recovered density model. In the implementation of the algorithm, the regularization parameter (μ ; Tikhonov and Arsenin, 1977) is varied to determine an optimal trade-off point between data misfit (ϕ_d ; Eq (2)) and the model objective function (ϕ_m ; Eq (3)). A graphical plot for the data misfit versus the model objective function, called a Tikhonov curve, or L-curve (Calvetti et al., 2000), is then used to determine the optimal regularization parameter, which is normally located at the corner of the plotted L-curve.

In the 3-D tesseroid inversion approach of Zhang et al. (2018), the objective function is implemented in spherical coordinate (Liang et al., 2014), unlike the ordinary Cartesian coordinate (Li and Oldenburg, 1996, 1998), thereby taking into consideration the curvature of the sphere (Eq (4)). This is achieved through replacing the uniform prism cells by spherical cells in the depth weighting function, in which the spherical cells are rescaled to the same level.

$$[G^T W_d^T W_d G + \mu W_m^T W_m] m = G^T W_d^T W_d d^{obs} + \mu W_m^T W_m m_{ref} \quad (4)$$

where, G^T , W_d^T and W_m^T are transpose matrices for the G , W_d and W_m . Then, geological/geophysical constraints that defines the physical characteristics of the real world and other constraints that controls the inversion process are included in a form of the Lagrangian multiplier (Eq (5); Rockafellar, 1970; Zhang et al., 2015, 2018), thereby increasing the reliability and dependability of the inversion density results. The implemented approach of this algorithm is defined by Zhang et al. (2015, 2018) and indicated in Eq (5),

$$\begin{aligned} & \left[G^T W_d^T W_d G + \mu W_m^T W_m + \frac{1}{2} M(F_1 + F_2 + F_3) \right] m = G^T W_d^T W_d d^{obs} + \mu W_m^T W_m m_{ref} \\ & - F_0 \lambda_0^T + F_1 \lambda_1^T + F_2 \lambda_2^T + \frac{1}{2} M(F_0 m_0 + F_1 m_1 + F_2 m_2) + \frac{1}{2} M(F_1 Z_1^2 - F_2 Z_2^2) \end{aligned} \quad (5)$$

where, the diagonal of the matrix F_i denotes the index of the constrained information in each divided rectangle cell, M is the penalty factor, λ represents Lagrangian multipliers, and Z_i is the slack variable of the i th cell, where i is the index number for each cell that represents defined

geological/geophysical bounds constraints.

3.3. Inversion parameters

The residual Bouguer gravity anomaly generally reflects the bulk density distributions in the crust. As such, we created a 3-D mesh based on the published geological and geophysical data in eastern Botswana. The published crustal models for the region do not show variable crustal layering with density contrasts. However, based on the presence of prominent deep (~14 km) sedimentary basins in central and western Botswana e.g., Passarge and Nosop basins (Fig. 1), we envision a crustal layer in which certain localized domains would have an appreciable density contrast with the underlying crystalline basement. Thus, a 3-D mesh was prepared as a single crustal layer, which contains varying density structures (Table 1).

The choice of parameters used includes the accepted optimal values for the Earth (1–11 in Table 2; Zhang et al. (2015) and those defined in this study (12–16 in Table 2). The base of the 3-D mesh, which represents a flat Moho, was set to 50 km, the deepest point along the Moho obtained from seismic studies in eastern Botswana (station NE218 of Fadel et al., 2018, Fig. 1b). Where the Moho is shallower than the base of the 3D mesh, the inversion tends to assign average density values beneath the true Moho. The inversion discretizes the gravity anomaly into 3-D density distribution in the 3-D mesh cells of unknown density anomaly. The initial density value for each cell was set to zero (0) kg/m³ to obtain density contrast values relative to the average density. The cell size in the radial direction was discretized into cell sizes of 2 km. This avoids the introduction of artifacts when the cell value is small and smearing effect associated with large cell values (e.g., Chisenga, 2020). The penalty factor was assigned a small value of 1.0×10^{-6} (with an increment of 2) and iteratively increased until the penalty factor fits the constrained information (Zhang et al., 2015). The depth weighting value of 2, adopted from previous studies (Zhang et al., 2015, 2018), optimally solves the clustering of density values close to the surface and counteracts the decay of gravity signal that led to a uniform distribution of density anomalies with depth. Then, the density value in each cell was allowed to vary between -150 kg/m³ and $+450$ kg/m³, based on the discretized gravity anomaly in each cell.

These values represent upper and lower density bounds based on the density of rocks in Eastern Botswana values (~2500 kg/m³ and 3100 kg/m³; Key and Ayres, 2000) relatively to average density of ~2650 kg/m³. Although the lower crust has a relatively higher average density (~2700 kg/m³), the difference is taken care of by the upper bound value, as noticed in the study of Zhang et al. (2018). One of the problems with gravity inversion is the non-uniqueness associated with multiple solutions for the same data. We minimized this problem by inverting the data several times and estimating an optimal regularization parameter (Tikhonov and Arsenin, 1977) in the objective parameter (Eq. (1); Fig. 3). The L-curve (Fig. 3) indicates an optimal regularization parameter of 2.5, which produce a desirable density model that also fits the Bouguer gravity data.

Table 1
The 3-D mesh and dataset for inversion.

Region	Inversion range	Model		Data	
		Grid size	Grid number	Data size	Data number
Eastern Botswana	Longitude	0.1°	112	0.1°	112
	Latitude	0.1°	112	0.1°	112
	Depth	0–50 km		0–50 km	
	Radial direction	2 km	26	2 km	26

Table 2
Final parameters for the density inversion.

number	Parameter	Value
1	Roughness factor in the x, y and z direction	2, 2, 2
2	Length scale	$1.0e^{-10}$
3	Depth weighting parameter	2
4	Penalty factor	$1e^{-6}$
5	Increase number for penalty factor	2
6	Convergence threshold of the inversion	$1e^{-4}$
7	Maximum iteration number of the inversion	1000
8	Convergence threshold of the CG method	$1e^{-8}$
9	Maximum iteration number of the CG method	500
10	x-y cell size	As indicated in Table 1
11	Radial direction cell size	2 km
12	Upper density bound	-150 kg/m^3
13	Lower density bound	$+450 \text{ kg/m}^3$
14	3D mesh base extent	50 km
15	Regularizing parameter	2.5

3.4. 3-D thermo-mechanical geodynamic model

To test strain localization in a region consisting of crustal blocks with contrasting densities, we simulate a time dependent 3-D thermo-mechanical numerical model of continental extension based on the results of the gravity inversion density model of the study area (see section 3.3). We use the open-source finite element code ASPECT v2.4 (Advanced Solver for Problems in the Earth's Convection; Bangerth and Heister, 2015; Bangerth et al., 2020; Heister et al., 2017). The ASPECT software package is used to solve for the Stokes flow equation for highly viscous incompressible fluid and has been successful for studying tectonic extension and normal fault network development (e.g., Glerum et al., 2018; Naliboff et al., 2020; Rajaonarison et al., 2020; Neuharth et al., 2022). In typical continental rifting models, extension is initiated using outward velocity boundary condition on the eastern and western boundaries of the model domain and by applying randomly distributed plastic strain weakening in the model center to localize deformation.

In our numerical modeling experiment, since the goal is to test the first order influence of juxtaposed low- and high-density blocks on the localization of crustal deformation within a normal faulting stress regime, we do not use plastic strain weakening mechanisms to help localize strain. Typical continental extension models (e.g., Naliboff et al., 2020) incorporate strain weakening mechanism (through the use of random seeds) to study rift evolution up to break-up stage, but those are out of the scope of this study. Similarly, our model does not

incorporate sedimentation, magmatism, and plasticity. Considering the large computational cost required for the model run, we purposefully stop the model at 2 Ma when it represents sufficient time to show that deformation has maintained localization in the model.

The model domain is $200 \times 150 \times 150$ km along the horizontal (x- and y-axis) and vertical (z-axis) respectively, for a box geometry (Fig. 4a). Using the 3-D gravity inversion results as model constraint, the initial density model consists of a 35-km thick crust with relatively high-density blocks of 2750 kg/m^3 separated by a relatively low-density central region of 2650 kg/m^3 (between 75 km and 125 km along the x axis) (Fig. 4a); a 65 km-thick mantle lithosphere and 50-km thick sub-lithospheric mantle, both assigned a density of 3300 kg/m^3 . The initial temperature and viscosity model follows Naliboff et al. (2020) and Rajaonarison et al. (2020) from which, the initial temperature of the lithosphere is a conductive geothermal gradient characteristic of the continental lithosphere, calculated as function of lithospheric thinness, and crustal thicknesses, while the lithospheric viscosity follows a dislocation creep rheology with brittle failure consistent with the Druker Prager criterion.

Since the lithospheric structure is uniform across the model (35-km thick crust and 100-km thick lithosphere), the imposed crustal density contrast causes lateral viscosity variation (function of density, temperature, and pressure) where relatively low viscosity occurs at the relatively lower-density regions (see Fig. 4b). The velocity boundary condition consists of a 5 mm/yr outward extensional velocity applied at the East and West faces of the model domain that is compensated with inward velocity at the bottom of the model, and tangential velocity at the South and North faces, and free surface at the top of the model.

4. Results

4.1. Bouguer gravity structural edges in the 2017 Mw6.5 epicentral region

In the edge-filtered (the raw derivative and low-pass derivative-filtered) Bouguer anomaly grids of eastern Botswana (Fig. 2c-d), systematic patterns of rectilinear-to-curvilinear gradients are observable. Although the raw vertical derivative map (Fig. 2c), which corresponds to shallow crustal levels, is dominated by gradients that are discontinuous along their strike, the low-pass derivative filtered map (Fig. 2d) which corresponds to deeper (>15 km depth) crustal levels, shows more laterally continuous gradients.

Within the Limpopo Belt, the gradients generally show a NW-SE trend which rotate into a NE-SW to NNE-SSW trend in the Magondi

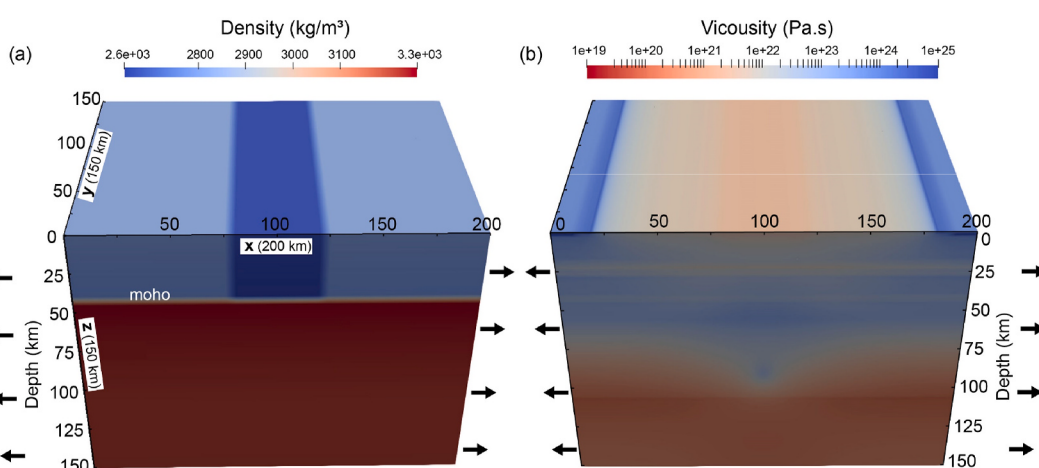


Fig. 4. (a) Initial density model of a time dependent 3-dimensional (3-D) thermo-mechanical model of continental deformation in a normal faulting stress regime, adopted in this study to test strain localization in a crust of heterogeneous density. Note that the alternating crustal blocks of contrasting density are constrained by the results of the 3-D gravity inversion performed in this study (see sections 3.3 and 4.1). (b) Viscosity model resulting from the imposed crustal density contrast (viscosity varies laterally as a function of density, temperature, and pressure). Note the relatively low viscosities occurring at the relatively lower-density regions.

Belt to the northwest. In both the Zimbabwe and Kaapvaal cratons, multiple structural trends emerge but appear to show a diffused pattern. More importantly, the epicenter of the 2017 Mw6.5 earthquake is collocated with a prominent NW-trending >270 km-long gravity gradient boundary which is most pronounced and continuous at deeper crustal levels (Fig. 2d). The southwestern flank of this gradient boundary is generally characterized by a high-gravity anomaly and the northeastern flank by a lower gravity gradient.

4.2. The 3-D density structure of eastern Botswana

The 3-D density structure beneath Eastern Botswana obtained from Bouguer gravity data (e.g., Fig. 5a) shows heterogeneous crustal densities varying between 2500 kg/m³ and 3000 kg/m³ (Fig. 5b–f). The anomalies in the crust (5–20 km) are characterized by short wavelengths with high amplitudes (e.g., Fig. 5b–d). These high frequency anomalies are significantly attenuated at the 30–40 km depths (Fig. 5e and f). At these deeper depths only a few isolated regions of high density remain, and they are localized either at the edges or interior of the cratons (e.g., most observable in the 30 km map). The highest density anomaly occurs at the boundary between the Zimbabwe Craton and the NMZ. Similarly, other high-density anomalies (albeit to a lesser extent) occur at the boundary between the Kaapvaal Craton and the SMZ (Fig. 5e and f).

4.3. Density structure of the 2017 Mw 6.5 Botswana earthquake epicentral region

Fig. 6a shows the horizontal slice of the density anomaly of the epicentral region at 20 km depth overlaid with the interpreted faults

from Kolawole et al. (2017) and earthquake aftershocks (obtained from Midzi et al. (2018)). At a depth of 20 km, the 2017 Mw6.5 Botswana earthquake epicenter region is characterized by a NW-trending ~65 km-wide zone of high-density (>2720 kg/m³) anomalies within the SMZ. This block is separated from the flanking domains of lower densities (<2640 kg/m³) by prominent density contrast boundaries. The southwestern boundary of this high-density block aligns with the trace of the Dinokwe thrust which separates the SMZ from the Kaapvaal Craton to the southwest; whereas the 2017 Mw6.5 mainshock and aftershocks cluster along the northeastern boundary of the block (Fig. 6a). Also, the density contrast boundaries collocate and align with the prominent gradients that are observable in the filtered gravity maps (Fig. 2c–d, and 6b).

In cross-sectional view, the density blocks continue to deeper depth levels in the crust (Fig. 7a–b), a common issue with density inversions. However, we note that in contrast to the flanking blocks where the density anomalies disappear more rapidly with depth, the central high-density block in the epicenter region dissipates more gently with depth (Fig. 7b). In the vertical section, orthogonal to the earthquake cluster, the hypocenter distribution of the earthquakes defines a primary, steeply dipping NE cluster that aligns with the northeast boundary of the high-density block (Fig. 7a–b). Further to the northeast, a steep, narrow SW-dipping zone of moderate density contrast anomaly (~2700 kg/m³) extends down-section to merge with the prominent density contrast boundary at depth (Fig. 7b). We note that the projected depth location of the mainshock hypocenter (24–29 km) is collocated with the intersection zone of these density contrast boundaries.

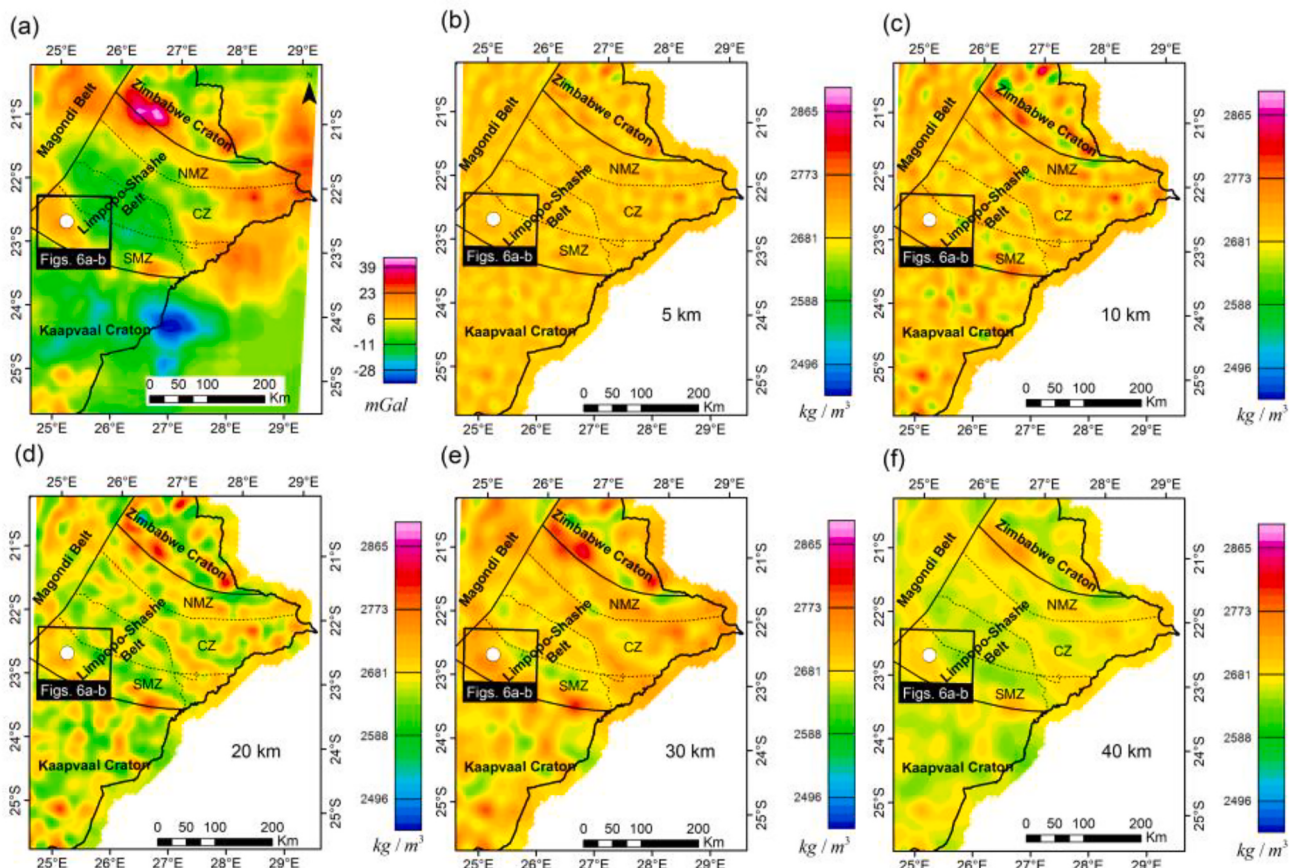


Fig. 5. (a) Residual Bouguer anomaly map of eastern Botswana after the application of a 1000 km Butterworth high pass filter. Horizontal slices from the 3-dimensional (3-D) density cube inversion model at (b) 5 km, (c) 10 km, (d) 20 km, (e) 30 km, and (f) 40 km. White circle = mainshock epicentre of the 2017 Botswana earthquake.

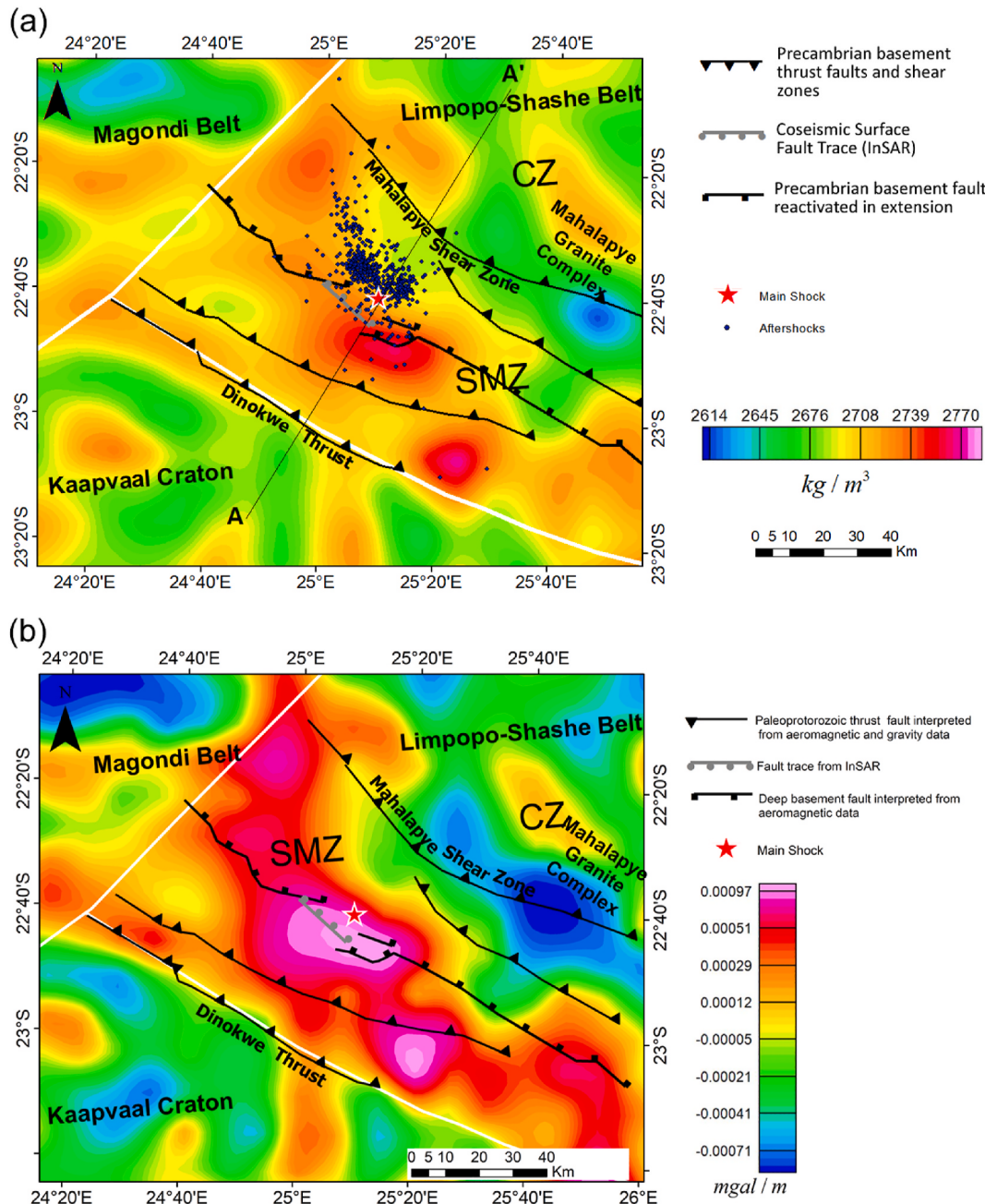


Fig. 6. (a) 20 km horizontal depth slice through the 3-dimensional (3-D) density cube inversion model covering the epicentral region of the Mw6.5 Botswana earthquake, overlaid with published basement fault interpretations (Kolawole et al., 2017) and aftershocks (Midzi et al., 2018). (b) First vertical derivative of the Bouguer gravity anomaly map of the epicentral area (see the regional-scale version of the map in Fig. 2c).

4.4. Geodynamic model results and interpretation

The result of the 3-D geodynamic model is presented as strain rate field at 2 Ma (Fig. 8), where relatively high strain rates in the crust and mantle lithosphere indicate brittle deformation, and thus, can be regarded as faults. Due to the imposed tensional forces, normal faults develop in the model, defining half grabens and grabens (small rift basins). As expected, the normal fault networks trend parallel to the rift axis or perpendicular to the extensional velocity, and they develop in the crust (or lithosphere) across the model domain. The observed off-rift normal and the associated conjugate faults is as a result of slightly distributed strain due to the absence of plastic strain weakening in the model center. However, the model result shows relatively higher strain rate faults in the model center and the highest strain rate faults coincide

with both the eastern and western boundaries of contrasting density crustal blocks. The development of relatively high strain rate faults at those interfaces indicates that those boundaries represent the weakest part of the model which promote strain concentration.

5. Discussion

5.1. Subsurface structure of the 2017 Mw6.5 Botswana earthquake fault

The 3-D density inversion model and edge-filtered gravity gradient maps (Fig. 2c-s, 6a-b, and 7a-b) reveal a prominent deep-reaching NW-trending, NE-dipping contrast boundary that shows striking coincidence and spatial alignment with the earthquake clusters in both map-view and dip-view. This prominent density contrast boundary coincides

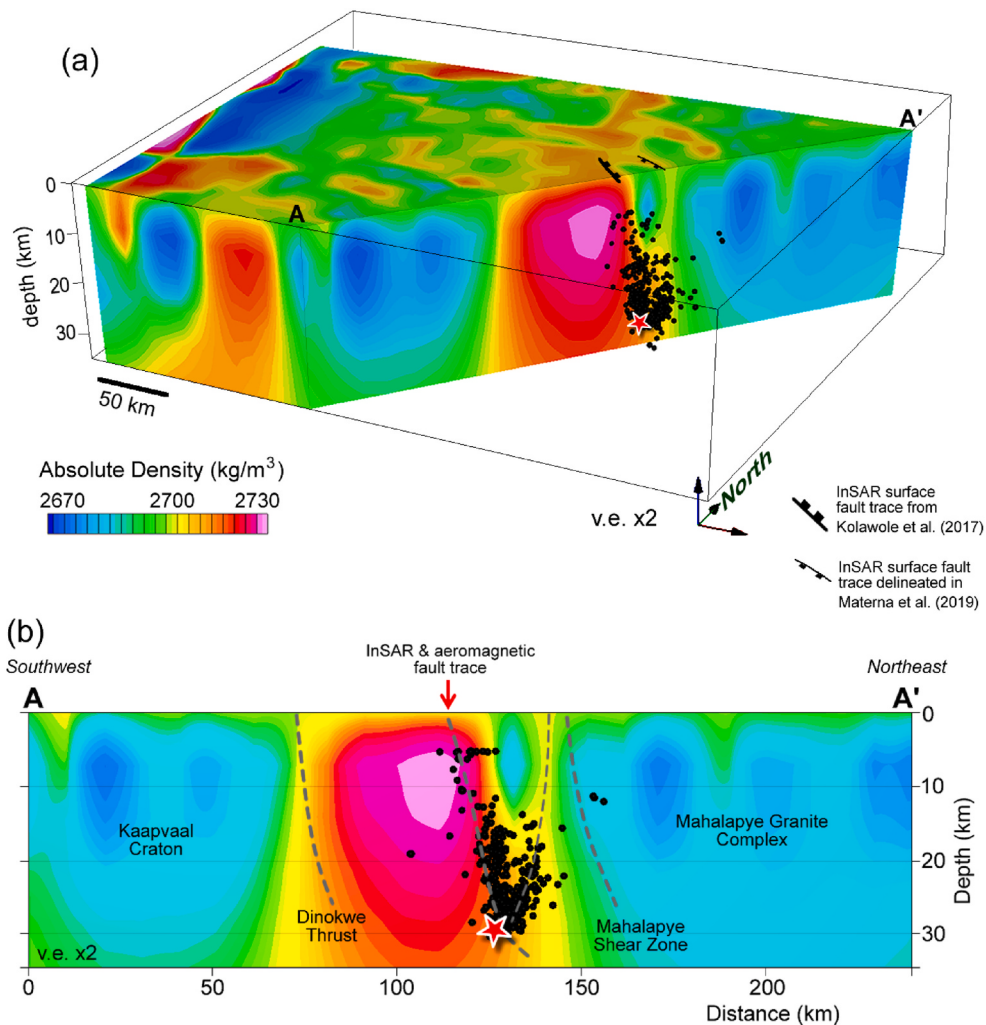


Fig. 7. (a) 3-D density cube inversion model of the area in Fig. 6a. (b) NE-SW cross-section through the density inversion model (see Fig. 6a for cross-section transect). The colour scale applies to both panels a and b.

with the location and geometry of previously published InSAR and aeromagnetic fault trace of the fault that ruptured the 2017 Mw6.5 Botswana earthquake, dubbed the “Moiyabana Lineament” or “Moiyabana Fault” (Kolawole et al., 2017). This fault also coincides with the inferred zone of displaced high-conductivity layer at the hypocenter (Moorkamp et al., 2019, 2020) and is colinear with a cluster of NW-trending Holocene normal fault scarps further southeast in South Africa (Mulabisana et al., 2021). Although the magnitude of density contrast across this structure decreases through the hypocenter region in the lower crust (Fig. 7a–b), previous results of 3-D aeromagnetic inversion across the ruptured fault (Kolawole et al., 2017) shows a basement discontinuity that is collocated with the density contrast boundary and extends down through the hypocenter depth region.

Sediment thickness distribution across the epicenter area, estimated from boreholes (Linol, 2013) show anomalous thickness of the Kalahari Sand across the Moiyabana Fault (Kolawole et al., 2017) where the sediments attain a maximum thickness of ~210 m. This indicates that there is no significant basement subsidence in the hanging wall, suggesting that the density contrast across the Moiyabana Fault is not due to normal fault offset. Thus, we interpret the prominent density contrast boundary is an inherited basement structure that is undergoing brittle reactivation by the Moiyabana Fault in the present-day normal faulting stress regime.

Further, our results reveal a minor, SW-dipping density contrast in the hanging wall of the master fault that coincides with a splay in the

aftershock distribution (Fig. 5b). We suggest that the rupture of this master fault triggered secondary rupture on a sub-parallel minor antithetic fault that dips to the SW. This antithetic fault coincides with the location and trend of a SW-dipping InSAR fault trace that Materna et al. (2019) posited as the main master fault (Figs. 6a and 7b). Based on the results of this current study, we suggest that the 2017 Mw6.5 Botswana earthquake represents the reactivation of multiple pre-existing Precambrian basement faults. The reactivated master fault is NW-trending/NE-dipping (Kolawole et al., 2017) and sub-parallel antithetic (minor) faults accommodated some of the aftershocks. Also, we observe that the mainshock hypocenter plots at a lower crustal region (24–29 km) where the density contrast boundaries merge at depth (Fig. 7a–b), suggesting that the mainshock nucleated near a fault intersection.

Elsewhere, the down-dip interaction of intersecting faults, as delineated by aftershock clusters, has been proposed to be the cause of an Mw5-to-6 earthquake sequence and energetic aftershock series (2009 Karonga earthquake; Gaherty et al., 2019). Although the 2017 Botswana earthquake produced dense aftershock series that reactivated multiple fault strands, the event was a normal foreshock–main shock–aftershock sequence, and the aftershocks dominantly occurred at shallower crustal levels (Fig. 7a–b). Thus, we suggest that the mainshock ruptured a master fault, the Moiyabana Fault, and that the aftershock distribution may be attributed to either 1.) static stress redistribution into the surrounding regions (static Coulomb stress change transfer) such that a

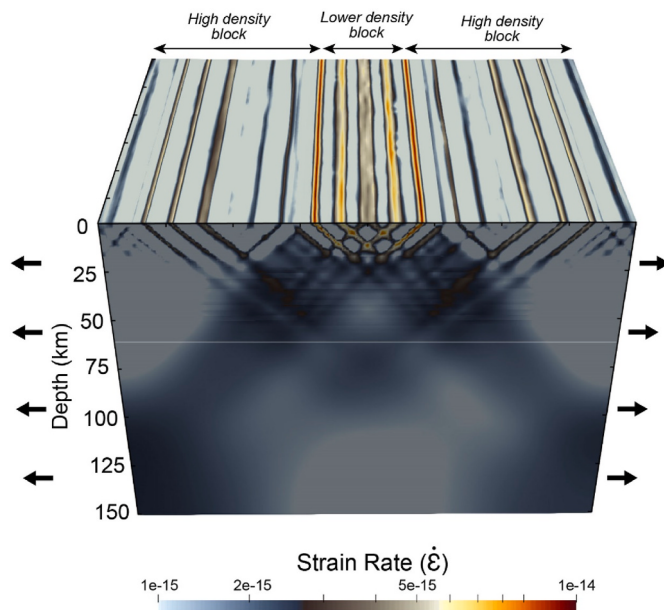


Fig. 8. The three-dimensional (3-D) strain field of a lithospheric block testing strain distribution around crustal density contrast boundaries without using plastic strain weakening mechanism. The result shows that the highest strain concentrates on the faults that follow the density contrast boundaries.

positive stress change develops at a shallower crustal level in the hanging wall of the Moiyabana Fault (e.g., Galderisi and Galli, 2020), 2.) possible fluid diffusion into the hanging wall of the master fault, or 3.) a combination of both mechanisms.

5.2. Localization of intraplate earthquakes at faulted density contrast boundaries

The collocation of the ruptured fault with a large (>270 km-long) density contrast boundary presents a large mechanical contrast boundary where stresses and strain may have preferentially concentrated in the crust (Fig. 9). The 3-D thermomechanical model of strain

distribution across a crust containing density contrast boundaries shows that such boundaries are effective concentrators of strain (Figs. 8 and 9). However, we note that the geodynamic model presented in our study incorporates long-term strain accumulation on faults as a failure mechanism, which is only representative of active plate boundaries and not stable intraplate regions due to low tectonic loading rates in plate interiors (e.g., Calais et al., 2016). Although geodetic crustal stretching rates in southern Africa is considerably low (Saria et al., 2014; Wedmore et al., 2021), the region is anything but stable due to the active African Superplume in its mantle (e.g., Gurnis et al., 2000). Thus, we propose the strain concentration idea as a plausible mechanism for seismogenic fault failure in eastern Botswana.

So long as differential stresses are high enough, minimal stress perturbations from external forces can easily bring the pre-stressed crustal faults to failure (Mandal, 2010). This is consistent with the designation of density contrast boundaries as stress concentrators in previous cases of intraplate earthquake ruptures (e.g., Mareschal and Kuang, 1986; Mandal et al., 1994; 1999; Shah et al., 2014). Elevated stresses that increase with depth have also been observed along earthquake nucleation zones associated with density contrasts (Mandal et al., 1994; 1999). For example, in the 1997 Mw5.8 Jabalpur earthquake of Central India, the stress differences due to crustal density heterogeneities was proposed to be the major contributor of the rock failure along a pre-existing weak zone (Mandal, 2010).

Additionally, large faulted mechanical contrast boundaries in the crust have been characterized as bi-material fault segments where asymmetrical dynamic fault rupture may occur (Ampuero and Ben-Zion, 2008; Ampuero and Ben-Zion, 2008; Dalguer and Day, 2009; Share and Ben-Zion, 2016). Talwani (2014) proposed a model for intraplate earthquakes in which local stress concentrators in both the upper and lower crust control the localization of stresses and elevated strain rates leading to intraplate fault rupture.

Therefore, in the case of the 2017 Mw6.5 Botswana earthquake, we suggest that although tectonic loading rates in such an intracratonic region are low (relative to active plate boundaries), the presence of a prominent deep-reaching density contrast boundary in the Moiyabana area, being favourably oriented to the tectonic stress field, represents a strain concentrator that could at the least, have partially facilitated the reactivation of the Moiyabana Fault (Fig. 9). Another prominent density contrast boundary in the region, the interpreted northern boundary of

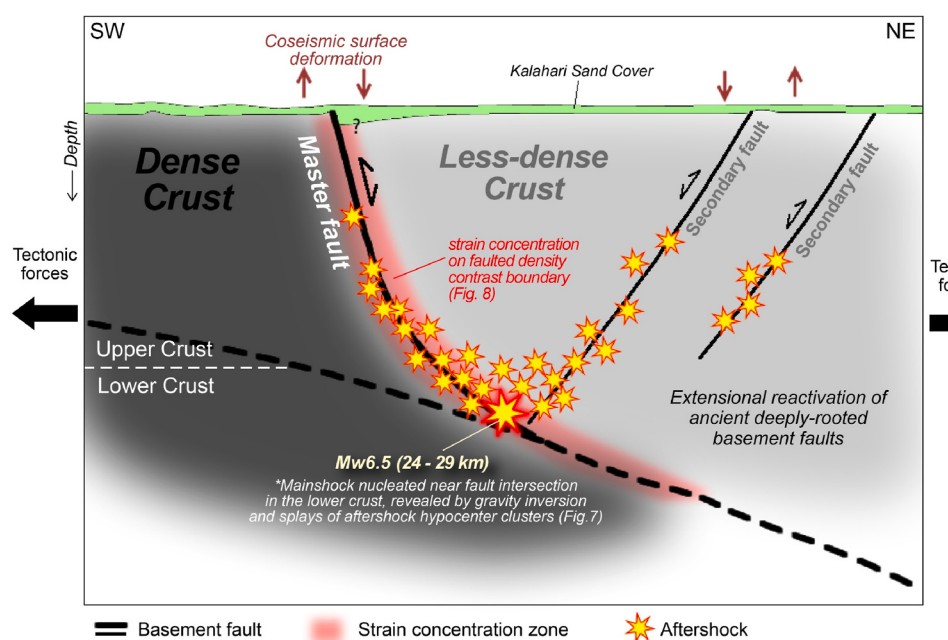


Fig. 9. Cartoon cross-section illustrating the main ruptured fault (master fault) as a NE-dipping structure that exploited a crustal density contrast boundary, and at least one antithetic (secondary) basement fault that was also reactivated within the epicentral area, both resolvable in the density inversion model and highlighted by aftershock distribution. The results suggest that the lower crustal 2017 Mw6.5 Botswana event localized along a fault that may be experiencing strain concentrations due to its association with the crustal-scale density contrast boundary.

the Kaapvaal Craton (dubbed ‘Dinokwe Thrust’; Figs. 5 and 6), did not show evidence of reactivation (i.e., seismicity). However, this could be due to a mis-orientation of its dip for brittle reactivation in the current normal faulting stress regime. Overall, it is important to note that although bulk crustal density contrast variation may localize high strain rates on a given fault segment, the mode of reactivation (i.e., seismic or aseismic) of such a fault segment is a complex frictional process and cannot be easily determined by density contrast gradients.

6. Conclusion

We performed a 3-D inversion of the gravity data to produce a density model of eastern Botswana with particular focus on the 2017 Mw 6.5 Botswana earthquake epicentral region. We present the results comparing dense aftershock hypocenter clusters with the crustal density structure, and test the geodynamic implications of the results with a representative 3-D thermomechanical model. We show that the ruptured fault is a NW-trending, NE-dipping fault that follows a deep-reaching density-contrast boundary, characterized by a high-density footwall to the southwest and low-density hanging wall to the northeast.

The integration of the 3-D density model and the aftershock hypocenter clusters reveal the presence of antithetic secondary fault splays that merge with the master fault at depth, where the mainshock hypocenter (24–29 km depth) is located near the zone of fault intersection. The results show that the earthquake event is associated with the brittle reactivation of multiple strands of pre-existing basement faults. Finally, the results of the 3-D thermomechanical testing of extensional strain distribution across density contrast boundaries demonstrate that so long as the magnitude of stress perturbation is high enough, faulted crustal-scale density contrast boundaries are preferential concentrators of strain, which may represent potential stress concentrators where intraplate earthquakes can localize.

Declaration of competing interest

The authors declare that they have no known competing financial interests or personal relationships that could have appeared to influence the work reported in this paper.

Data availability

The authors do not have permission to share data.

Acknowledgement

Gravity data used in this research is provided by the Geoscience Institute of Botswana. The right for data sharing solely remains with the institution but can be viewed online (<http://geoscienceportal.geosoft.com/Botswana/search>). The main shock and its fault plane solution were extracted from USGS website (<http://earthquake.usgs.gov/earthquakes/eventpage/us10008e3k/executive>). The aftershocks were part of the second scientific project of rapid installation of a temporary network of six seismograph in the epicentral area to record the aftershocks (Midzi et al., 2018). More than 500 aftershocks were recorded and analyzed by the Botswana Geoscience Institute (BGI) and Council for Geosciences of South Africa (CGS). The data is not yet made available in any repository but was provided to us by Vunganai Midzi upon request. We thank the editor R.B.M. Mapeo, and Ameha Muluneh and an anonymous reviewer for useful comments that helped to improve the quality of our manuscript. Also, we thank K. Leseane for a review of an earlier version of this manuscript.

References

- Albano, M., Polcari, M., Bignami, C., Moro, M., Saroli, M., Stramondo, S., 2017. Did anthropogenic activities trigger the 3 april 2017 Mw 6.5 Botswana earthquake? *Rem. Sens.* 9 (12), 1028. <https://doi.org/10.3390/rs9101028>.
- Ampuero, J., Ben-Zion, Y., 2008. Cracks, pulses and macroscopic asymmetry of dynamic rupture on a bimaterial interface with velocity-weakening friction. *Geophys. J. Int.* 173, 674–692. <https://doi.org/10.1111/j.1365-246X.2008.03736.x>.
- Balfour, N.J., Cummins, P.R., Pilia, S., Love, D., 2015. Localization of intraplate deformation through fluid-assisted faulting in the lower-crust: the Flinders Ranges. *Tectonics* 35, 97–106. <https://doi.org/10.1016/j.tecto.2015.05.014>.
- Bangerth, W., Dannberg, J., Gassmoller, R., Heister, T., 2020. ASPECT v2.2.0 [software]. <https://doi.org/10.5281/zenodo.3924604>.
- Bangerth, W., Heister, T., 2015. ASPECT: Advanced Solver for Problems in Earth's Convection Computational Infrastructure for Geodynamics.
- Begg, G.C., Griffin, W.L., Natapov, L.M., O'Reilly, S.Y., Grand, S.P., O'Neill, C.J., Hronsky, J.M.A., Djomani, Y.P., Swain, C.J., Deen, T., Bowden, P., 2009. The lithospheric architecture of Africa: seismic tomography, mantle petrology, and tectonic evolution. *Geosphere* 5 (1), 23–50. <https://doi.org/10.1130/GES00179.1>.
- Block, A.E., Bell, R.E., Studinger, M., 2009. Antarctic crustal thickness from satellite gravity: implications for the transantarctic and gamburtsev subglacial mountains. *Earth Planet. Sci. Lett.* 288 (1–2), 194–203. <https://doi.org/10.1016/j.epsl.2009.09.022>.
- Burg, J.P., 1975. Maximum Entropy Spectral Analysis. Unpubl Ph.D Thesis. Staford university.
- Calais, E., Camelbeeck, T., Stein, S., Liu, M., Craig, T.J., 2016. A new paradigm for large earthquakes in stable continental plate interiors, 621–10 *Geophys. Res. Lett.* 20 (10), 637. <https://doi.org/10.1002/2016GL070815>.
- Calvetta, D., Morigib, S., Reichel, L., Sgallarid, F., 2000. Tikhonov regularization and the L-curve for large discrete ill-posed problems. *J. Comput. Appl. Math.* 123, 423–446. [https://doi.org/10.1016/S0377-0427\(00\)00414-3](https://doi.org/10.1016/S0377-0427(00)00414-3).
- Chen, W.P., Molnar, P., 1983. Focal depths of intracontinental and intraplate earthquakes and their implications for the thermal and mechanical properties of the lithosphere. *J. Geophys. Res. Solid Earth* 88, 4183–4214.
- Chisenga, C., 2020. Local geodynamic model and layer structure for enhancing understanding of the earth and lunar dynamics. PhD Thesis. In: Wuhan University Press. Wuhan University.
- Chisenga, C., Van der Meijde, M., Yan, J., Fadel, I., Atekwana, E.A., Steffen, R., Ramotoko, C., 2020a. Gravity derived crustal thickness model of Botswana: its implication for the Mw 6.5 April 3, 2017, Botswana earthquake. *Tectonophysics* 787, 228479.
- Chisenga, C., Yan, J., Zhao, J., Atekwana, E.A., Steffen, R., 2020b. Density structure of the rümker region in the northern oceanus procellarum: implications for lunar volcanism and landing site selection for the chang'E-5 mission. *J. Geophys. Res.: Planets* 125 (1). <https://doi.org/10.1029/2019JE005978>.
- Chisenga, C., Yan, J., Zhao, J., Deng, Q., Barriot, J.-P., 2019. Density structure of the von kármán crater in the Northwestern south Pole-aitken basin: initial subsurface interpretation of the Chang'E-4 landing site region. *Sensors* 19 (20), 4445. <https://doi.org/10.3390/s19204445>.
- Clifford, T.N., 1970. The structural framework of Africa. In: Clifford, T.N., Gass, I.G. (Eds.), *African Magmatism and Tectonics*. Oliver and Boyd, pp. 1–26.
- Dalguer, L.A., Day, S.M., 2009. July. Asymmetric Rupture of Large Aspect-Ratio Faults at Bimaterial Interface in 3D, vol. 36, pp. 1–5. <https://doi.org/10.1029/2009GL040303>.
- Fadel, I., Meijde, M., Van Der, Paulsen, H., 2018. Crustal structure and dynamics of Botswana, 659–10 *J. Geophys. Res. Solid Earth* 123 (10), 671. <https://doi.org/10.1029/2018JB016190>.
- Fadel, I., Paulsen, H., van der Meijde, M., Kwadiba, M., Ntibinyane, O., Nyblade, A., Durheim, R., 2020. Crustal and upper mantle shear wave velocity structure of Botswana: the 3 April 2017 central Botswana earthquake linked to the East African Rift System. *Geophys. Res. Lett.* 47 (4), e2019GL085598.
- Gaherty, J.B., Zheng, W., Shillington, D.J., Pritchard, M.E., Henderson, S.T., Chindandali, P.R.N., Mdala, H., Shuler, A., Lindsey, N., Oliva, S.J., Nooner, S., 2019. Faulting processes during early-stage rifting: seismic and geodetic analysis of the 2009–2010 Northern Malawi earthquake sequence. *Geophys. J. Int.* 217 (3), 1767–1782.
- Galderisi, A., Galli, P., 2020. Coulomb stress transfer between parallel faults. The case of Norcia and Mt Vettore normal faults (Italy, 2016 Mw 6.6 earthquake). *Results in Geophysical Sciences* 1, 100003.
- Gardonio, B., Jolivet, R., Calais, E., Lecl, H., 2018. The April 2017 M w 6 . 5 Botswana earthquake : an injective event triggered by deep fluids. *Geophys. Res. Lett.* <https://doi.org/10.1029/2018GL078297>. April 2017.
- Glerum, A., Thieulot, C., Fraters, M., Blom, C., Spakman, W., 2018. Nonlinear viscoplasticity in ASPECT: benchmarking and applications to subduction. *Solid Earth* 9 (2), 267–294.
- Gurnis, M., Mitrovica, J.X., Ritsema, J., van Heijst, H.J., 2000. Constraining mantle density structure using geological evidence of surface uplift rates: the case of the African superplume. *G-cubed* 1 (7).
- Heister, T., Dannberg, J., Gassmoller, R., Bangerth, W., 2017. High accuracy mantle convection simulation through modern numerical methods-II: realistic models and problems. *Geophys. J. Int.* 210 (2), 833–851.
- Hough, S.E., Seeber, L., Armbruster, J.G., 2003. Intraplate triggered earthquakes: observations and interpretation. *Bull. Seismol. Soc. Am.* 93 (5), 2212–2221.
- Jackson, J., 2002. Strength of the continental lithosphere: time to abandon the jelly sandwich? *GSA Today (Geol. Soc. Am.)* 12, 4–9.

- Jackson, J., McKenzie, D., Priestley, K., Emmerson, B., 2008. New views on the structure and rheology of the lithosphere. *Journal of Geological Society of London* 165, 453–465.
- Jansen, J.C., Andrews-Hanna, J.C., Li, Y., Lucey, P.G., Taylor, G.J., Goossens, S., Lemoine, F.G., Mazarico, E., Head, J.W., Milbury, C., Kiefer, W.S., Soderblom, J.M., Zuber, M.T., 2017. Small-scale density variations in the lunar crust revealed by GRAIL. *Icarus* 291, 107–123. <https://doi.org/10.1016/j.icarus.2017.03.017>.
- Johnston, A.C., 1996. Seismic moment assessment of earthquakes in stable continental regions—II. Historical seismicity. *Geophys. J. Int.* 125, 639–678.
- Johnston, Arch C., Schweig, E.S., Churchill, W., 1996. The enigma of the new Madrid earthquake of 1811–1812. *Annu. Rev. Earth Planet Sci.* 24, 339–384.
- Kanamori, H., Brodsky, E.E., 2004. The physics of earthquakes. *Rep. Prog. Phys.* 67 (8), 1429–1496.
- Key, R.M., Ayres, N., 2000. The 1998 edition of the National geological map of Botswana. *J. Afr. Earth Sci.* 30 (3), 427–451. [https://doi.org/10.1016/S0899-5362\(00\)00030-0](https://doi.org/10.1016/S0899-5362(00)00030-0).
- Khoza, T.D., Jones, A.G., Muller, M.R., Evans, R.L., Miensopust, M.P., Webb, S.J., 2013. Lithospheric structure of an Archean craton and adjacent mobile belt revealed from 2-D and 3-D inversion of magnetotelluric data : example from southern Congo craton in northern Namibia. *J. Geophys. Res.* 118, 4378–4397. <https://doi.org/10.1002/jgrb.50258>.
- Kolawole, F., Atekwana, E.A., Malloy, S., Stamps, D.S., Grandin, R., Abdelsalam, M.G., Leseane, K., Shemang, E.M., 2017. Aeromagnetic, gravity, and differential interferometric synthetic aperture radar analyses reveal the causative fault of the 3 april 2017 Mw 6.5 moyibana, Botswana, earthquake. *Geophys. Res. Lett.* 44 (17), 8837–8846. <https://doi.org/10.1002/2017GL074620>.
- Kolawole, F., Atekwana, E.A., Laó-Dávila, D.A., Abdelsalam, M.G., Chindandali, P.R., Salima, J., Kalindekafe, L., 2018. Active deformation of Malawi rift's north basin Hinge zone modulated by reactivation of preexisting Precambrian Shear zone fabric. *Tectonics* 37 (3), 683–704.
- Lawson, C.L., Hanson, R.J., 1974. Solving Least Squares Problem. Prentice-Hall.
- Leseane, K., Atekwana, E.A., Mickus, K.L., Abdelsalam, M.G., Shemang, E.M., Atekwana, E.A., 2015. Thermal perturbations beneath the incipient Okavango Rift zone, northern Botswana. *J. Geophys. Res. Solid Earth* 120, 1210–1228. <https://doi.org/10.1002/2014JB011029>.
- Li, Y., Oldenburg, D., 1998. 3-D inversion of gravity data. *Geophysics* 63 (1), 264–267.
- Li, Yaoguo, Oldenburg, D.W., 1996. 3-D inversion of magnetic data. *Geophysics* 61 (2), 394–408.
- Mandal, P., 2010. Three-dimensional modeling of intraplate stresses in the epicentral zone of the 21 May 1997 Jabalpur earthquake of Mw 5.8, central India. *Tectonophysics* 485, 1–8.
- Mandal, P., Manglik, A., Singh, R.N., 1994. Intraplate stresses along a section of the kavali-udipi dss profile in the south indian shield induced by density heterogeneities and topography. *J. Geodyn.* 17 (4), 203–211.
- Liang, Q., Chen, C., Li, Y., 2014. 3-D inversion of gravity data in spherical coordinates with application to the GRAIL data. *J. Geophys. Res. Planets* 119 (6), 1359–1373. <https://doi.org/10.1002/2014JE004626>.
- Linol, B., 2013. Sedimentology and sequence stratigraphy of the Congo and Kalahari basins of south Central Africa and their evolution during the formation and break-up of west Gondwana. PhD Thesis. Nelson Mandela Metropolitan University, Port Elizabeth.
- Mandal, Prantik, 1999. Intraplate Stress Distribution Induced by Topography and Crustal Density Heterogeneities beneath the South Indian Shield , India, vol. 302, pp. 159–172.
- Mandal, Prantik, 2010. Tectonophysics Three-dimensional modeling of intraplate stresses in the epicentral zone of the 21 May 1997 Jabalpur earthquake of M w 5 . 8 , central India. *Tectonophysics* 485 (1–4), 1–8. <https://doi.org/10.1016/j.tecto.2009.11.011>.
- Mandal, Prantik, Pandey, O.P., 2010. Relocation of aftershocks of the 2001 Bhuj earthquake: a new insight into seismotectonics of the Kachchh seismic zone, Gujarat, India. *J. Geodyn.* 49 (5), 254–260. <https://doi.org/10.1016/j.jog.2010.01.005>.
- Mareschal, J.-C., Kuang, J., 1986. Intraplate stresses and seismicity : the role of topography and density heterogeneities. *Tectonophysics* 132, 153–162.
- Materna, K., Wei, S., Wang, X., Heng, L., Wang, T., Chen, W., Salman, R., Bürgmann, R., 2019. Source characteristics of the 2017 M w 6 . 4 Mojabana , Botswana earthquake , a rare lower-crustal event within an ancient zone of weakness. *Earth Planet Sci. Lett.* 506, 348–359. <https://doi.org/10.1016/j.epsl.2018.11.007>.
- McCaffrey, R., 1989. Teleseismic investigation of the january 22, 1988 tennant Creek, Australia, earthquakes. *Geophys. Res. Lett.* 16 (5), 413–416. <https://doi.org/10.1029/GL016i005p00413>.
- McCourt, S., Vearncombe, J.R., 1992. Shear zones of the Limpopo Belt and adjacent granitoid-greenstone terranes: implications for late Archaean collision tectonics in southern Africa. *Precambrian Res.* 55, 553–570.
- Midzi, V., Saunders, I., Manzunu, B., Kwadiba, M.T., Zulu, S., Jele, V., Mantsha, R., Marimira, K.T., Mulabisana, T.F., Ntibinyane, O., Pule, T., Rathod, G.W., Sitali, M., Tabane, L., Van, G., 2018. The 03 April 2017 Botswana M6.5 earthquake: preliminary results. *J. Afr. Earth Sci.* 143, 187–194. <https://doi.org/10.1016/j.jafrearsci.2018.03.027>.
- Miensopust, M.P., Jones, A.G., Muller, M.R., Garcia, X., Evans, R.L., 2011. Lithospheric Structures and Precambrian Terrane Boundaries in Northeastern Botswana Revealed through Magnetotelluric Profiling as Part of the Southern African Magnetotelluric Experiment, vol. 116, pp. 1–21. <https://doi.org/10.1029/2010JB007740>.
- Miller, H.G., Singh, V., 1994. Semiquantitative techniques for the removal of directional trends from potential field data. *J. Appl. Geophys.* 32 (2–3), 199–211. [https://doi.org/10.1016/0926-9851\(94\)90021-3](https://doi.org/10.1016/0926-9851(94)90021-3).
- Moorkamp, M., Fishwick, S., Walker, R.J., Jones, A.G., Mt, C., 2019. Geophysical evidence for crustal and mantle weak zones controlling intra-plate seismicity – the 2017 Botswana earthquake sequence. *Earth Planet Sci. Lett.* 506, 175–183. <https://doi.org/10.1016/j.epsl.2018.10.048>.
- Moorkamp, M., Atekwana, E., Fadel, I., Gabriel, A.A., Kolawole, F., Shemang, E., Ramotokoro, C., van der Meijde, M., Mickus, K., Selengen, A., Molwalefhe, L., 2020. Integrated geophysical analysis of the April 2017 Moiyabana intra-plate earthquake, Botswana. In: EGU-general Assembly 2020 Abstract # EGU2020-9241.
- Mulabisana, T., Meghraoui, M., Midzi, V., Saleh, M., Ntibinyane, O., Kwadiba, T., Manzunu, B., Seiphembo, O., Pule, T., Saunders, I., 2021. Seismotectonic analysis of the 2017 moyabana earthquake (MW 6.5; Botswana), insights from field investigations, aftershock and InSAR studies. *J. Afr. Earth Sci.* 182, 104297.
- Naliboff, J.B., Glerum, A., Brune, S., Péron-Pinvidic, G., Wrona, T., 2020. Development of 3-D rift heterogeneity through fault network evolution. *Geophys. Res. Lett.* 47 (13).
- Neuharth, D., Brune, S., Wrona, T., Glerum, A., Braun, J., Yuan, X., 2022. Evolution of rift systems and their fault networks in response to surface processes. *Tectonics* 41 (3), e2021TC007166.
- Paulussen, H., Micallef, T., Bouwman, D.R., Ruigrok, E., Herman, M.W., Fadel, I., van der Meijde, M., Kwadiba, M., Maritinkole, J., Ntibinyane, O., 2022. Rifting of the Kalahari craton through Botswana? New seismic evidence. *J. Geophys. Res. Solid Earth* 127 (4), e2021JB023524.
- Rajaonarison, T.A., Stamps, D.S., Fishwick, S., Brune, S., Glerum, A., Hu, J., 2020. Numerical modeling of mantle flow beneath Madagascar to constrain upper mantle rheology beneath continental regions. *J. Geophys. Res. Solid Earth* 125 (2), e2019JB018560.
- Ranganai, R.T., Kampunzu, A.B., Atekwana, E.A., Paya, B.K., King, J.G., Koosimile, D.I., Stettler, E.H., 2002. Gravity evidence for a larger Limpopo Belt in southern Africa and geodynamic implications. *Geophys. J. Int.* 149 (3) <https://doi.org/10.1046/j.1365-246X.2002.01703.x>.
- Rockafellar, R.T., 1970. Convex Analysis. Princeton University Press.
- Roering, C., Reenen, D. D. Van, Smit Jr., C.A., J. M.B., Beer, J. H. De, Wit, M. J. De, 1992. Tectonic model for the evolution of the Limpopo belt. *Precambrian Res.* 55, 539–552. [https://doi.org/10.1016/0301-9268\(92\)90044-0](https://doi.org/10.1016/0301-9268(92)90044-0).
- Salem, A., Williams, S., Fairhead, J.D., Smith, R., Ravat, D., 2007. Interpretation of magnetic data using tilt-angle derivatives. *Geophysics* 73 (1), L1–L10.
- Saria, E., Calais, E., Stamps, D.S., Delvaux, D., Hartnady, C.J.H., 2014. Present-day kinematics of the east African Rift. *J. Geophys. Res. Solid Earth* 119 (4), 3584–3600.
- Shah, A.K., Horton, J.W., Burton, W.C., Spears, D.B., Gilmer, A.K., 2014. Subsurface geologic features of the 2011 central Virginia earthquakes revealed by airborne geophysics. *GSA Special Paper* 509.
- Share, P.E., Ben-Zion, Y., 2016. Bimaterial interfaces in the South San Andreas Fault with opposite velocity contrasts NW and SE from San Gorgonio Pass. *Geophys. Res. Lett.* 43 (20), 10–680. <https://doi.org/10.1002/2016GL070774>.
- Shi, F., Wang, Y., Yu, T., Zhu, L., Zhang, J., Wen, J., Gasc, J., Incel, S., Schubnel, A., Li, Z., Chen, T., 2018. Lower-crustal earthquakes in southern Tibet are linked to eclogitization of dry metastable granulite. *Nat. Commun.* 9 (1), 3483.
- Singletary, S.J., Hanson, R.E., Martin, M.W., Crowley, J.L., Bowring, S.A., Key, R.M., Ramokate, L.V., Direng, B.B., Krol, M.A., 2003. Geochronology of basement rocks in the Kalahari Desert, Botswana, and implications for regional Proterozoic tectonics. *Precambrian Res.* 121 (1–2), 47–71. [https://doi.org/10.1016/S0301-9268\(02\)00201-2](https://doi.org/10.1016/S0301-9268(02)00201-2).
- Sykes, L.R., 1978. Intraplate seismicity, reactivation of preexisting zones of weakness, alkaline magmatism, and other tectonism postdating continental fragmentation. *Rev. Geophys.* 16 (4), 621–688.
- Talwani, P., 2014. Intraplate Earthquakes. Cambridge university press.
- Tesauro, M., Kaban, M.K., Mooney, D.W., 2015. Variations of the lithospheric strength and elastic thickness in North America. *G-cubed* 16, 2197–2220. <https://doi.org/10.1002/2015GC005937.Received>.
- Tikhonov, A.N., Arsenin, V.Y., 1977. Solutions of Ill-Posed Problems. Winston and Sons. USGS, 2016. M5.9 Northern Tanzania Earthquake of 10 September 2016. USGS Publication.
- Wedmore, L.N., Biggs, J., Floyd, M., Fagereng, Å., Mdala, H., Chindandali, P., Williams, J.N., Mphepo, F., 2021. Geodetic constraints on cratonic microplates and broad strain during rifting of thick Southern African lithosphere. *Geophys. Res. Lett.* 48 (17), e2021GL093785.
- Winograd, S., 1978. On computing the discrete fourier Transform. *Math. Comput.* 32 (141), 175–199.
- Winograd, S., 1979. On the multiplicative complexity of the discrete fourier Transform. *Adv. Math.* 32 (2), 83–117. [https://doi.org/10.1016/0001-8708\(79\)90037-9](https://doi.org/10.1016/0001-8708(79)90037-9).
- Yu, Y., Liu, K., Moidaki, M., Mickus, K., Atekwana, E.A., Gao, S.S., 2015. A joint receiver function and gravity study of crustal structure beneath the incipient Okavango Rift, Botswana. *Geophys. Res. Lett.* 42 (20), 8398–8405.
- Zhang, Y., Wu, Y., Yan, J., Wang, H., Rodriguez, J.A.P., Qiu, Y., 2018. 3D inversion of full gravity gradient tensor data in spherical coordinate system using local north - oriented frame. *Earth Planets Space.* <https://doi.org/10.1186/s40623-018-0825-5>.
- Zhang, Y., Yan, J., Li, F., Chen, C., Mei, B., Jin, S., Dohm, J.H., 2015. A new bound constraints method for 3-D potential field data inversion using Lagrangian multipliers. *Geophys. J. Int.* 201, 267–275. <https://doi.org/10.1093/gji/ggv016>.